

Experimental Realization of Type-II Weyl Points and Fermi Arcs in Phononic CrystalBoyang Xie,¹ Hui Liu,¹ Hua Cheng,^{1,2,*} Zhengyou Liu,³ Shuqi Chen,^{1,2,4,†} and Jianguo Tian^{1,2,4}¹*The Key Laboratory of Weak Light Nonlinear Photonics, Ministry of Education, School of Physics and TEDA Institute of Applied Physics, Nankai University, Tianjin 300071, China*²*The collaborative Innovation Center of Extreme Optics, Shanxi University, Taiyuan, Shanxi 030006, China*³*Key Laboratory of Artificial Micro- and Nanostructures of Ministry of Education and School of Physics and Technology, Wuhan University, Wuhan 430072, China*⁴*Renewable Energy Conversion and Storage Center, Nankai University, Tianjin 300071, China*

(Received 21 October 2018; published 14 March 2019)

Weyl points (WPs), as the doubly degenerate points in three-dimensional momentum band structures, carry quantized topological charges and give rise to a variety of extraordinary properties, such as robust surface wave and chiral anomaly. Type-II Weyl semimetals, which have conical dispersions in Fermi surfaces and a strongly tilted dispersion with respect to type I, have recently been proposed in condensed-matter systems and photonics. Although the type-II WPs have been theoretically predicted in acoustics, the experimental realization in phononic crystals has not been reported so far. Here, we experimentally realize a type-II Weyl phononic crystal. We demonstrate the topological transitions observed at the WP frequencies and the topological surface acoustic waves between the Weyl frequencies. The experiment results are in good accordance with our theoretical analyses. Due to the violation of the Lorentz symmetry, the type-II WPs only exist in low energy systems. As the analog counterpart in classical waves, the phononic crystal brings a platform for the research of type-II WPs in macroscopic systems.

DOI: [10.1103/PhysRevLett.122.104302](https://doi.org/10.1103/PhysRevLett.122.104302)

Weyl points (WPs) as linear point degeneracies constitute the simplest nontrivial band structures in three-dimensional (3D) momentum space. Together with 3D Dirac points [1], line nodes [2–5] and weak topological insulators [6] in 3D topologically nontrivial systems, WPs have become a research focus in the field of 3D topological phases. Recently, Weyl fermions have been discovered in Weyl semimetals [7–10], giving rise to a variety of extraordinary properties, such as robust surface waves [7] and chiral anomalies [11]. The type-II Weyl fermions are fundamentally new to the type-I Weyl fermions, which host a strongly tilted cone dispersion and possess a conical Fermi surface from contact between an electron and a hole pocket [7,12,13], in contrast to a point-like Fermi surface possessed by the type-I Weyl fermions. The Lifshitz transitions are also the characteristics of type-II WPs, which describe the topological transitions at the Fermi surface. As a consequence of topological changes at the Fermi surface, gapless surface states known as Fermi arcs emerge on the surfaces of a bulk sample, which connect the projections of bulk band pockets enclosing the type-II WPs. Unlike the type-I case, the type-II WPs can not exist in high-energy physics in Weyl's prediction [14] because they violate the Lorentz symmetry, which requires physical laws to be independent of the reference frame. These distinctions of two types of Weyl semimetals lead to different responses to magnetic fields and other physical properties [15,16].

The concept of nontrivial topological physics in solid-state systems has been extended to photonic [17–19] and phononic systems [20–22], with particular interests focusing on achieving one-way backscattering-immune surface states. WPs as fundamental topological band structures have soon been discovered in systems of electromagnetic waves [2,23–25], mechanical waves [5,25,26], and acoustic waves [27–29]. Acoustic Weyl phonons and Fermi arcs have been theoretically predicted [30,31], and experimentally observed in chiral phononic crystals [27–29]. The latest works have also focused on the influence of boundary conditions as well as the novel applications in negative refraction [28] and collimation effect [29]. The Weyl phonons in acoustic wave systems are different from those in condensed matter systems [32,33]. The acoustic wave systems do not contain transverse branches, but do contain the longitude branches in the band structure. The acoustic phonons are of low energy; hence they can hardly couple with electronic or magnetic field, electrons, and photons. The macroscopic nature and simpler band structure of phononic crystals have extraordinary advantages in experimentally exploring complex quantum physics. The type-II WPs in classical systems were predicted and observed in chiral hyperbolic metamaterials [34], photonic crystals [35–38], and magnetized plasma [39,40] from microwaves to optical waves. Acoustic type-II WPs have also been predicted with stacked graphene-based structures [30] and dimerized chains [31].

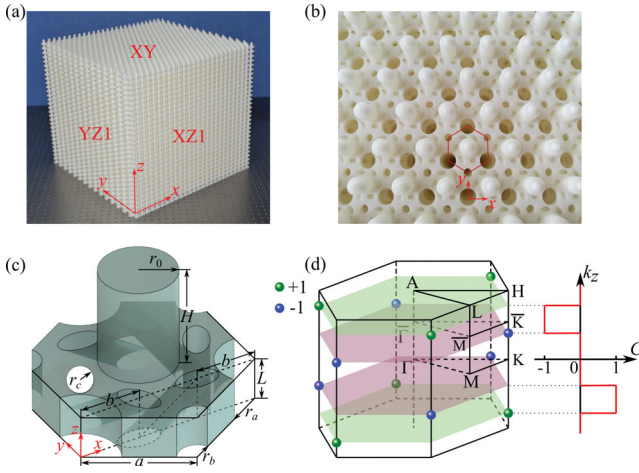


FIG. 1. The Weyl phononic crystal and its unit cell. (a) An image of the experimental sample. (b) Magnified image of the top view. A unit cell is outlined with red hexagon. (c) Geometry of the unit cell. (d) The first bulk BZ of the Weyl phononic crystal. The olive and blue spheres label WPs with opposite charges. The red solid line on the right side shows the Chern number of the 2D band with a fixed k_z .

Although the type-II WPs have been theoretically predicted in acoustics, there still lacks experimental realization and observation for deeper insight.

Here, we report on the experimental realization of acoustic type-II WPs in a stacked graphene-like chiral phononic crystal. The experimental results clearly exhibit the characteristics of type-II WPs by observing conical dispersion and the Lifshitz transition at Fermi frequencies. As a signature of topological phase transition, the band gap closing and reopening in a reduced two-dimensional (2D) Brillouin zone (BZ) are observed. We also show the existence of acoustic Fermi arcs, which connect the bulk bands that enclose WPs of opposite charges. All observations are in good agreement with the theoretical analyses. Compared with the nonchiral type-II photonic [37] or phononic crystals [31], the chirality in phononic crystal is crucial to the observation of Fermi arcs between the type-II WPs.

The type-II Weyl phononic crystal consists of stacked layers with broken inversion symmetry. Figure 1(a) provides a photo of our sample, showing the stacked structured plates fabricated by 3D printing. The magnified top view of the sample together with an outline of the unit cell is shown in Fig. 1(b). The schematic of the hexagonal unit cell is shown in Fig. 1(c). Each unit consists of a central pillar supported by the perforated plate. The pillars between two successive plates form an in-plane waveguide with a triangular lattice. At the corners of the unit cells, two interlaced triangular lattices of tubes connect the two neighboring waveguides. Six slanted cylindrical tubes are symmetrically distributed around the central axis of each pillar in a spiral pattern. The unit cell has the side length $a = 12.75$ mm, and the central pillar has a radius of $r_0 = 4.5$ mm and a height

of $H = 12$ mm. The plate has a thickness of $L = 5.25$ mm. The experimental sample has a cuboid geometry with a size of 574.1 mm \times 573.7 mm \times 517.5 mm. The tubes at the unit corners have the radius $r_a = 4.5$ mm and $r_b = 2.25$ mm. The slanted tubes around the central pillar have the radius $r_c = 1.5$ mm. The central axis of the slanted tubes lies in the same plane as the central axis of the vertical tubes. The tilt angle from x - y plane is $\text{atan}[L/(\sqrt{3}a - 2b)] = 36^\circ$ for the slanted tubes. The hollow waveguides and channels are all filled with air, and the structure is considered acoustically rigid. The space of the in-plane waveguide can be viewed as graphene-like metastructure with meta-atoms at the corners of the unit cells, similar to the resonance cavities connected by tubes [30]. Each in-plane waveguide supports 2D linear dispersions for acoustic modes with touching points at the corners of the 2D first BZ. When we stack the waveguides and connect them with vertical tubes with $r_a \neq r_b$, the type-II WPs can exist in the high symmetric KH ($K'H'$) line [or referred to as the \bar{K} (\bar{K}') point] of the BZ. Although the type-II WPs can exist without chiral coupling, the one-way surface acoustic waves (SAWs) are unobservable in the experiment. This is because the topological charges of WPs cancel out through projection to the surfaces, and the WPs share the same frequency that the topological transitions at Fermi surfaces also cancel out (Supplemental Material [41]). Therefore, we add the chiral coupling between the two successive waveguides so that the WPs in \bar{K}/\bar{K}' point move downward or upward to different k_z planes due to mirror symmetry breaking of y - z plane. The frequency of the WPs with topological charge -1 or $+1$ will have a redshift or blueshift. If the chiral coupling is too strong, the WPs become type I [41]. Another possible approach to realize a Weyl phase transition from type I to type II and the mirror symmetry breaking is to utilize a synthetic frequency dimension created by dynamic modulation [38], but it is hard to be realized in acoustics.

The behavior of the acoustic system can be predicted by a two band tight-binding model [30]. The Hamiltonian of the model can be written in the Pauli matrix form

$$H(\mathbf{k}) = d_0 I + d_x \sigma_x + d_y \sigma_y + d_z \sigma_z. \quad (1)$$

The WP can only exist along the KH ($K'H'$) lines of the BZ where $d_x = d_y = 0$. The first term tilts the band dispersion in k_z direction. The band dispersion along KH is $E_1 = \varepsilon_b + 2t_b \cos(k_z h) + 6t_c \sin(k_z h - \pi/6)$ and $E_2 = \varepsilon_a + 2t_a \cos(k_z h) - 6t_c \sin(k_z h + \pi/6)$, where ε_a and ε_b represent the sublattice on-site energy. t_a , t_b are the interlayer nonchiral hopping tuned by r_a , r_b , and t_c is the interlayer chiral hopping tuned by r_c , respectively. The type-II WPs can be achieved with $\varepsilon_1 \approx \varepsilon_2$, $t_a \neq t_b$ and a small t_c at the crossing of the two bands. The effective Hamiltonian around the WP is

$$H(\delta\mathbf{k}) = \sum \delta k_i v_{ij} \sigma_j, \quad i, j \in \{x, y, z\}, \quad (2)$$

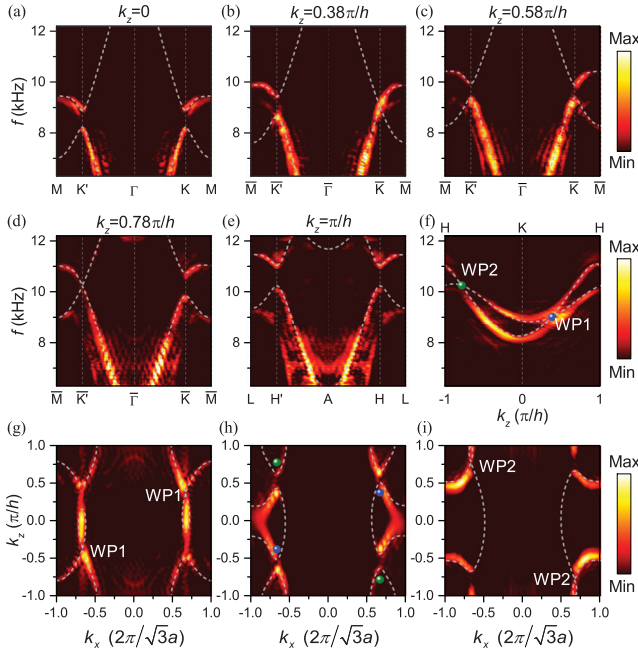


FIG. 2. Bulk bands of the two lowest modes. (a)–(e) In planes (a) $k_z = 0$, (b) $0.38\pi/h$, (c) $0.58\pi/h$, (d) $0.78\pi/h$, (e) π/h , and (f) along the KH direction. (g)–(i) The Fermi surface at $k_y = 0$ for different frequencies. (g) 9036 Hz is set to the lower-frequency WP1. Contact between electron and hole pockets occurs at WP1. (h) 9600 Hz is set to be between the two WPs. The two band pockets are disconnected. WP1 is enclosed by one of the bands. The positions of WP1 and WP2 are denoted by blue and olive spheres. (i) 10268 Hz is set to the higher-frequency WP2, two band pockets touch again at WP2. The amplitudes represent the strength of the states stimulated in the phononic crystal.

where v_{ij} are the group velocities. The topological charges (or chirality) for WPs are $c = \text{sgn}[\det(v_{ij})] = \pm 1$ as shown in Fig. 1(d). The details of the tight-binding model are demonstrated in the Supplemental Material [41].

To confirm the existence of the WPs, we show the bulk band dispersions for the Weyl phononic in Figs. 2(a)–2(f). The color maps represent the experimental dispersions obtained by Fourier transforming measured pressure fields inside the sample (experiment methods are shown in the Supplemental Material [41]), and the gray dashed lines denote the calculated values obtained from full wave simulations. Simulation results of the two lowest-order acoustic bands have shown that two groups of type-II WPs exist as shown in Fig. 2(f): WP1 with $c = -1$ lies in \bar{K} point with $k_z = 0.38\pi/h$ and its time-reversal counterpart in \bar{K}' point with $k_z = -0.38\pi/h$ at $f = 9036$ Hz, which is denoted with blue spheres in Fig. 1(d); WP2 with $c = 1$ lies in \bar{K} point with $k_z = -0.78\pi/h$ and its time-reversal counterpart in \bar{K}' point with $k_z = 0.78\pi/h$ at $f = 10268$ Hz, which is denoted with olive spheres in Fig. 1(d). For k_z planes $0.38\pi/h < k_z < 0.78\pi/h$ or $-0.78\pi/h < k_z < -0.38\pi/h$ [between the light green and red planes in Fig. 1(d)], the reduced 2D BZ has a nontrivial Chern number

-1 or $+1$, respectively. The calculation of topological charges is given in the Supplemental Material [41]. Two bands degenerate at WPs with linear dispersion and the cone spectrum near the WPs is strongly tilted for k_z direction.

For different k_z planes, the reduced 2D bands will undergo the band closing and reopening process. We measured the 2D band structures to observe the band closing and reopening process by fixing k_z planes. In $k_z = 0$ plane, the two lowest bands are gapped [Fig. 2(a)]. Without the effective gauge flux arising from a nonzero k_z , the Chern number of 2D BZ is zero. With the increasing value of k_z , at $k_z = 0.38\pi/h$, the two bands degenerate at \bar{K} point with linear dispersion [Fig. 2(b)]. The 2D bands reopen and then close at \bar{K}' with $k_z = 0.78\pi/h$ [Fig. 2(d)]. For a greater k_z , the bands reopen again in the 2D BZ. The 2D bands in $k_z = 0$, $k_z = 0.58\pi/h$ and $k_z = \pi/h$ planes are gapped as shown in Figs. 2(a), 2(c) and 2(e) for comparison. The band closing and reopening indicate that, in k_z planes with $0.38\pi/h < k_z < 0.78\pi/h$, the Chern number of 2D band is $+1$ or -1 . Some parts of the Bloch modes are better stimulated, which result in brighter colors along the theoretical lines. For example, the states of $\bar{K}\bar{M}$ and $\bar{\Gamma}\bar{K}$ have different symmetries, which lead to some distinctions in the coupling efficiency and amplitude. The Fermi surfaces are shown in Figs. 2(g)–2(i) with $k_y = 0$. Topological transition of the Fermi surface is observed, which is also known as Lifshitz transitions [7]. At frequencies below WP1, the two bands form separate equipfrequency contours as the band pockets. When the Fermi frequency is tuned to WP1, $f = 9036$ Hz, the two band pockets touch at the position of WP1, as illustrated in Fig. 2(g). A further increase of frequency splits the pockets, but the topology changes because WP1 is enclosed by one of the bands [Fig. 2(h) for $f = 9600$ Hz]. The band pockets touch again [Fig. 2(i) for $f = 10268$ Hz] when the Fermi surface is tuned to the higher-frequency WP2, which leads to another topology change. Further increase of Fermi frequency disconnects the band pockets again. The simulation result is well confirmed by the experiment. The real space data of 9036 Hz are shown in the Supplemental Material [41], Movie 1.

When the frequency is tuned to be between the WPs, the Fermi arc states appear in XZ and YZ surfaces. Owing to time-reversal symmetries, the WPs of opposite chirality are projected on top of each other; hence no topologically protected surface states appear in XY surfaces. The SAWs of type-II WPs stay in an incomplete band gap. The Fermi arcs of type-II Weyl phononic crystal connect the bulk bands when the Fermi arcs are open curves in type-I Weyl phononic crystal. To map out the Fermi arc on the XZ or YZ surfaces, we use rigid cover plates with a zigzag or an armchair shape as trivial insulators for sound, respectively, and place a sound source close to the surface center for excitation. Figures 3(a) and 3(b) show the excited field on the $XZ1$ and $YZ1$ surfaces of the sample at 9600 Hz. The SAWs exhibit two main branches: the up- and right-ward

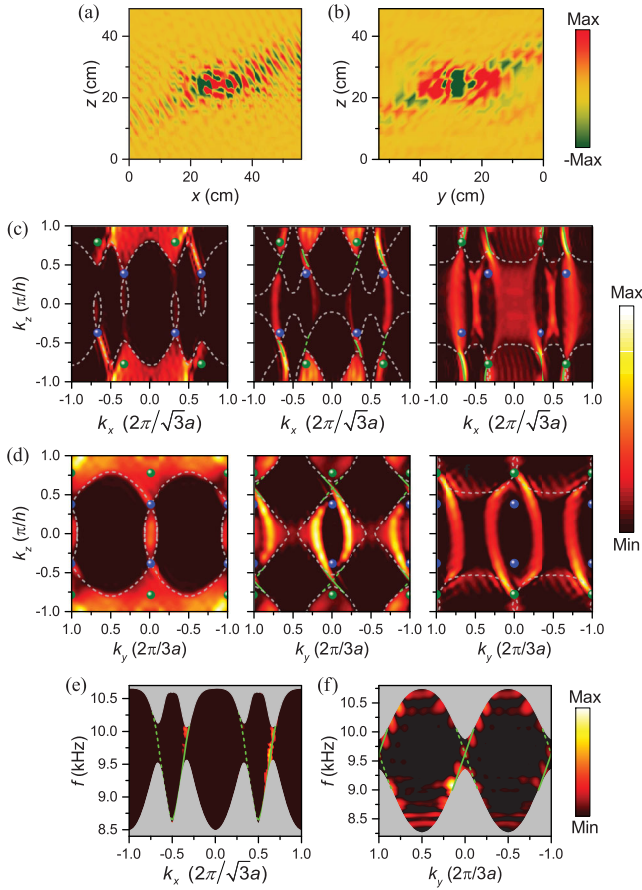


FIG. 3. Observation of topological SAWs. SAWs are excited by point sources placed at the center of the surfaces. (a) and (b) The temporal pressure field of (a) XZ1 and (b) YZ1 surfaces at 9600 Hz. (c) and (d) Fourier transforms of the SAW fields on the (c) XZ1 and (d) YZ1 surfaces, showing the equifrequency contours in the extended surface BZ at the WP1 frequency 9036 Hz (left), 9600 Hz (middle), and the WP2 frequency 10 268 Hz (right). (e) and (f) Surface band dispersion of $k_z = 0.6\pi/h$ for (e) XZ1 and (f) YZ1 surfaces. The gray dashed lines represent the outlines of the projected bulk bands. The positions of projected WP1 and WP2 are denoted by blue and olive spheres. The grey regions display the projected bulk bands. The green solid and dashed lines represent the simulated SAWs and the results on opposite surfaces.

propagation branch and the down- and left-ward propagation branch, which are related by time-reversal symmetry. The asymmetric propagation of sound is also a signature of Fermi arcs that appear with the WPs. We map out the measured Fermi surfaces in Figs. 3(c) and 3(d) for XZ1 and YZ1 surfaces, respectively. As the projected bulk bands have mirror symmetry in the YZ surfaces, we can distinguish the Fermi arcs apart from the bulk bands. We can also recognize the Fermi arc according to the band behavior near projected WPs.

At the WP1 frequency 9036 Hz [left in Figs. 3(c) and 3(d)], the projected bulk band pockets touch at WP1, which

can be clearly seen at YZ1 surface. The Fermi arcs emerge from WP1 and disappear in the bulk bands enclosing WP2. Although the whole SAWs are immersed in the bulk bands, we observed that the SAWs still contain considerable amount of amplitude. As we increase the Fermi frequency to 9600 Hz [middle in Figs. 3(c) and 3(d)] between the Weyl frequencies, the bulk bands split and the incomplete band gaps around $k_z = \pm 0.6\pi/h$ emerge. In the gap areas, the Fermi arcs emerge from a band pocket enclosing the projection of WP1 to another band pocket enclosing the projection of WP2. This result is in accordance with the Lifshitz transitions of bulk bands. Great agreement is found between the experiments (color scale) and simulations (green lines) for both surfaces. For comparison, we also show the calculated Fermi arcs of the surface states on the opposite surfaces XZ2 and YZ2 indicated by green dashed lines. The Fermi arcs contribute to the two main branches in Figs. 3(a) and 3(b). At the WP2 frequency 10 268 Hz [right in Figs. 3(c) and 3(d)], the bulk bands touch at WP2 while distinct SAWs emerge from the WP2 and disappear in the bulk bands enclosing WP1. The SAWs no longer propagate one directionally because of the extra SAW bands at the XZ1 surface. The SAWs of different frequencies share similar shapes. In Figs. 3(e) and 3(f) we present the experimental SAW dispersions for $k_z = 0.6\pi/h$, a topological nontrivial band appears in the band gap of the reduced 2D BZ. The result of YZ1 surfaces has a low resolution because of the limitation of finite-size effect. Overall, the experiment results are in good agreement with theoretical prediction and full-wave simulation. The refraction of SAW across XZ1 and YZ1 surfaces is directly observed in the Supplemental Material [41]. The surface states can be easily scattered into bulk states near the bulk bands. As an example shown in the nonchiral structure in Fig. S4 in the Supplemental Material, the surface states are greatly penetrated into the bulk. To enlarge the area of surface arcs, we can enlarge the gap between the bulk bands by increasing chiral coupling through bigger r_c or sublattice potential difference through a bigger r_a/r_b ratio in our design.

In conclusion, we designed and fabricated a Weyl phononic crystal that carries type-II WPs at the high-symmetry lines in the BZ. The 2D bands that were reduced by fixing k_z undergo the band closing and reopening process as k_z variates. We observed the topological transitions at the WP frequencies and the topological SAWs between the WP frequencies. Our Letter provides new insights to 3D topological acoustics and makes up the shortage of experimental work for type-II Weyl phononic crystal. While the Weyl phononic crystals are expected to be used to reduce reflections at the interfaces and sharp corners in low-loss devices, the type-II phononic crystals that host surface modes and bulk modes simultaneously might further broad the applications of Weyl phononic crystals in asymmetric waveguides and reflection-free anomalous refractions. We anticipate that our Letter may lead to potential applications of Weyl phononic crystals in advanced sound manipulation and may be extended to other systems including photonics and cold atoms [42].

This work was supported by the National Key Research and Development Program of China (Grants No. 2016YFA0301102 and No. 2017YFA0303800), the National Natural Science Foundation of China (Grants No. 91856101, No. 11574163, and No. 11774186), the Natural Science Foundation of Tianjin for Distinguished Young Scientists (18JCJQJC45700), the Natural Science Foundation of Tianjin (16JCQNJC01700), and the 111 Project (Grant No. B07013).

*hcheng@nankai.edu.cn

†schen@nankai.edu.cn

- [1] Q. Guo, B. Yang, L. Xia, W. Gao, H. Liu, J. Chen, Y. Xiang, and S. Zhang, Three Dimensional Photonic Dirac Points in Metamaterials, *Phys. Rev. Lett.* **119**, 213901 (2017).
- [2] L. Lu, L. Fu, J. D. Joannopoulos, and M. Soljačić, Weyl points and line nodes in gyroid photonic crystals, *Nat. Photonics* **7**, 294 (2013).
- [3] Q. Yan, R. Liu, Z. Yan, B. Liu, H. Chen, Z. Wang, and L. Lu, Experimental discovery of nodal chains, *Nat. Phys.* **14**, 461 (2018).
- [4] W. Gao, B. Yang, B. Tremain, H. Liu, Q. Guo, L. Xia, A. P. Hibbins, and S. Zhang, Experimental observation of photonic nodal line degeneracies in metacrystals, *Nat. Commun.* **9**, 950 (2018).
- [5] O. Stenull, C. L. Kane, and T. C. Lubensky, Topological Phonons and Weyl Lines in Three Dimensions, *Phys. Rev. Lett.* **117**, 068001 (2016).
- [6] A. Slobozhanyuk, S. H. Mousavi, X. Ni, D. Smirnova, Y. S. Kivshar, and A. B. Khanikaev, Three-dimensional all-dielectric photonic topological insulator, *Nat. Photonics* **11**, 130 (2017).
- [7] A. A. Soluyanov, D. Gresch, Z. Wang, Q. Wu, M. Troyer, X. Dai, and B. A. Bernevig, Type-II Weyl semimetals, *Nature (London)* **527**, 495 (2015).
- [8] X. Wan, A. M. Turner, A. Vishwanath, and S. Y. Savrasov, Topological semimetal and Fermi-arc surface states in the electronic structure of pyrochlore iridates, *Phys. Rev. B* **83**, 205101 (2011).
- [9] A. A. Burkov and L. Balents, Weyl Semimetal in a Topological Insulator Multilayer, *Phys. Rev. Lett.* **107**, 127205 (2011).
- [10] H. Weng, C. Fang, Z. Fang, B. A. Bernevig, and X. Dai, Weyl Semimetal Phase in Noncentrosymmetric Transition-Metal Monophosphides, *Phys. Rev. X* **5**, 011029 (2015).
- [11] X. Huang, L. Zhao, Y. Long, P. Wang, D. Chen, Z. Yang, H. Liang, M. Xue, H. Weng, Z. Fang, X. Dai, and G. Chen, Observation of the Chiral-Anomaly-Induced Negative Magnetoresistance in 3D Weyl Semimetal TaAs, *Phys. Rev. X* **5**, 031023 (2015).
- [12] K. Deng, G. Wan, P. Deng, K. Zhang, S. Ding, E. Wang, M. Yan, H. Huang, H. Zhang, Z. Xu, J. Denlinger, A. Fedorov, H. Yang, W. Duan, H. Yao, Y. Wu, S. Fan, H. Zhang, X. Chen, and S. Zhou, Experimental observation of topological Fermi arcs in type-II Weyl semimetal MoTe₂, *Nat. Phys.* **12**, 1105 (2016).
- [13] G. Chang, S.-Y. Xu, D. S. Sanchez, S.-M. Huang, C.-C. Lee, T.-R. Chang, G. Bian, H. Zheng, I. Belopolski, N. Alidoust, H.-T. Jeng, A. Bansil, H. Lin, and M. Z. Hasan, A strongly robust type II Weyl fermion semimetal state in Ta₃S₂, *Sci. Adv.* **2**, e1600295 (2016).
- [14] H. Weyl, Elektron und gravitation. I, *Z. Phys.* **56**, 330 (1929).
- [15] K. Deng, G. Wan, P. Deng, K. Zhang, S. Ding, E. Wang, M. Yan, H. Huang, H. Zhang, Z. Xu, J. Denlinger, A. Fedorov, H. Yang, W. Duan, H. Yao, Y. Wu, S. Fan, H. Zhang, X. Chen, and S. Zhou, Experimental observation of topological Fermi arcs in type-II Weyl semimetal MoTe₂, *Nat. Phys.* **12**, 1105 (2016).
- [16] T. E. O'Brien, M. Diez, and C. W. J. Beenakker, Magnetic Breakdown and Klein Tunneling in a Type-II Weyl Semimetal, *Phys. Rev. Lett.* **116**, 236401 (2016).
- [17] A. B. Khanikaev, S. H. Mousavi, W.-K. Tse, M. Kargarian, A. H. MacDonald, and G. Shvets, Photonic topological insulators, *Nat. Mater.* **12**, 233 (2013).
- [18] M. C. Rechtsman, J. M. Zeuner, Y. Plotnik, Y. Lumer, D. Podolsky, F. Dreisow, S. Nolte, M. Segev, and A. Szameit, Photonic Floquet topological insulators, *Nature (London)* **496**, 196 (2013).
- [19] J.-W. Dong, X.-D. Chen, H. Zhu, Y. Wang, and X. Zhang, Valley photonic crystals for control of spin and topology, *Nat. Mater.* **16**, 298 (2017).
- [20] Z. Yang, F. Gao, X. Shi, X. Lin, Z. Gao, Y. Chong, and B. Zhang, Topological Acoustics, *Phys. Rev. Lett.* **114**, 114301 (2015).
- [21] C. He, X. Ni, H. Ge, X.-C. Sun, Y.-B. Chen, M.-H. Lu, X.-P. Liu, and Y.-F. Chen, Acoustic topological insulator and robust one-way sound transport, *Nat. Phys.* **12**, 1124 (2016).
- [22] J. Lu, C. Qiu, L. Ye, X. Fan, M. Ke, F. Zhang, and Z. Liu, Observation of topological valley transport of sound in sonic crystals, *Nat. Phys.* **13**, 369 (2017).
- [23] K. Shastri, Z. Yang, and B. Zhang, Realizing type-II Weyl points in an optical lattice, *Phys. Rev. B* **95**, 014306 (2017).
- [24] L. Lu, Z. Wang, D. Ye, L. Ran, L. Fu, J. D. Joannopoulos, and M. Soljačić, Experimental observation of Weyl points, *Science* **349**, 622 (2015).
- [25] M. Fruchart, S.-Y. Jeon, K. Hur, V. Cheianov, U. Wiesner, and V. Vitelli, Soft self-assembly of Weyl materials for light and sound, *Proc. Natl. Acad. Sci. U.S.A.* **115**, E3655 (2018).
- [26] D. Z. Rocklin, B. G.-g. Chen, M. Falk, V. Vitelli, and T. C. Lubensky, Mechanical Weyl Modes in Topological Maxwell Lattices, *Phys. Rev. Lett.* **116**, 135503 (2016).
- [27] F. Li, X. Huang, J. Lu, J. Ma, and Z. Liu, Weyl points and Fermi arcs in a chiral phononic crystal, *Nat. Phys.* **14**, 30 (2017).
- [28] H. He, C. Qiu, L. Ye, X. Cai, X. Fan, M. Ke, F. Zhang, and Z. Liu, Topological negative refraction of surface acoustic waves in a Weyl phononic crystal, *Nature (London)* **560**, 61 (2018).
- [29] H. Ge, X. Ni, Y. Tian, S. K. Gupta, M.-H. Lu, X. Lin, W.-D. Huang, C. T. Chan, and Y.-F. Chen, Experimental observation of acoustic Weyl points and topological surface states, *Phys. Rev. Applied* **10**, 014017 (2018).
- [30] M. Xiao, W.-J. Chen, W.-Y. He, and C. T. Chan, Synthetic gauge flux and Weyl points in acoustic systems, *Nat. Phys.* **11**, 920 (2015).

- [31] Z. Yang and B. Zhang, Acoustic Type-II Weyl Nodes from Stacking Dimerized Chains, *Phys. Rev. Lett.* **117**, 224301 (2016).
- [32] T. Zhang, Z. Song, A. Alexandradinata, H. Weng, C. Fang, L. Lu, and Z. Fang, Double-Weyl Phonons in Transition-Metal Monosilicides, *Phys. Rev. Lett.* **120**, 016401 (2018).
- [33] H. Miao, T. T. Zhang, L. Wang, D. Meyers, A. H. Said, Y. L. Wang, Y. G. Shi, H. M. Weng, Z. Fang, and M. P. M. Dean, Observation of Double Weyl Phonons in Parity-Breaking FeSi, *Phys. Rev. Lett.* **121**, 035302 (2018).
- [34] B. Yang, Q. Guo, B. Tremain, L. E. Barr, W. Gao, H. Liu, B. Béri, Y. Xiang, D. Fan, A. P. Hibbins, and S. Zhang, Direct observation of topological surface-state arcs in photonic metamaterials, *Nat. Commun.* **8**, 97 (2017).
- [35] G. G. Pyrialakos, N. S. Nye, N. V. Kantartzis, and D. N. Christodoulides, Emergence of Type-II Dirac Points in Graphynelike Photonic Lattices, *Phys. Rev. Lett.* **119**, 113901 (2017).
- [36] J. Noh, S. Huang, D. Leykam, Y. D. Chong, K. P. Chen, and M. C. Rechtsman, Experimental observation of optical Weyl points and Fermi arc-like surface states, *Nat. Phys.* **13**, 611 (2017).
- [37] W.-J. Chen, M. Xiao, and C. T. Chan, Photonic crystals possessing multiple Weyl points and the experimental observation of robust surface states, *Nat. Commun.* **7**, 13038 (2016).
- [38] C. Qin, Q. Liu, B. Wang, and P. Lu, Photonic Weyl phase transition in dynamically modulated brick-wall waveguide arrays, *Opt. Express* **26**, 20929 (2018).
- [39] L. Xia, W. Gao, B. Yang, Q. Guo, H. Liu, J. Han, W. Zhang, and S. Zhang, Stretchable photonic fermi arcs in twisted magnetized plasma, *Laser Photonics Rev.* **12**, 1700226 (2018).
- [40] W. Gao, B. Yang, M. Lawrence, F. Fang, B. Béri, and S. Zhang, Photonic Weyl degeneracies in magnetized plasma, *Nat. Commun.* **7**, 12435 (2016).
- [41] See Supplemental Material at <http://link.aps.org/supplemental/10.1103/PhysRevLett.122.104302> for (i) the tight-binding model description of the system, (ii) type-II Weyl phononic crystal without chiral coupling, (iii) direct observation of the SAWs, and (iv) experimental methods.
- [42] W.-Y. He, S. Zhang, and K. T. Law, Realization and detection of Weyl semimetals and the chiral anomaly in cold atomic systems, *Phys. Rev. A* **94**, 013606 (2016).